Ionization balance in the negative glow of a Hg-Ar hot-cathode discharge

R. C. Wamsley, K. Mitsuhashi, and J. E. Lawler
Department of Physics, University of Wisconsin, Madison, Wisconsin 53706
(Received 24 November 1992)

Absorption spectroscopy is used to map the absolute density of excited Ar atoms and ground-state Hg^+ ions in the negative glow of a hot cathode Hg-Ar discharge. The experimental map of the density of excited Ar atoms is compared to, and found to agree with, a Monte Carlo simulation of the resonance-atom density from radiation trapping. The primary production rate per unit volume of excited Ar atoms in the simulation is sharply peaked near the cathode hot spot. The experimental map of the density of ground-state Hg^+ ions is compared to, and found to agree with, a simulation based on an ambipolar-diffusion model. The production rate per unit volume of Hg^+ in this second simulation is entirely due to Penning ionization of Hg by the excited Ar atoms. Penning ionization is found to be an important, possibly the dominant, ionization mechanism in the negative glow.

PACS number(s): 52.80.Hc, 52.25.Jm, 52.70.Kz, 52.25.Dg

I. INTRODUCTION

Glow discharges containing a mixture of Hg and Ar are widely used in fluorescent lighting and have been studied extensively. Sophisticated hydrodynamic models provide true predictive capability in the positive column of these discharges [1]. However, the cathode region, which includes the cathode fall, negative glow, and Faraday dark space, is not as well understood. Kinetic theory is best suited to describing this region because many of the standard hydrodynamic approximations fail in the cathode region. Modeling of the cathode region represents a difficult and fundamental challenge. Although the cathode region is not well understood, it is very important because cathodic phenomena limit the life of fluorescent lamps. New optical diagnostics and methods for numerical simulation can provide a very quantitative understanding to augment the existing more qualitative understanding [2].

In this paper we address the ionization balance of the negative-glow region in fluorescent lamps. Measurements of the absolute density of Ar atoms excited to the $3p^5 4s$ configuration (Ar*) and measurements of the absolute density of ground-state Hg^+ are reported. The spatial dependence of the Ar* density is sharply peaked near the cathode hot spot and has extended low "wings" throughout the negative glow. This spatial distribution is compared to Monte Carlo simulations of radiation trapping and is found to be controlled by resonance-radiation transport. Nearly all of the Ar* is produced by electron-impact excitation in a small region within approximately 1 mm of the cathode hot spot. The Ar* spreads throughout the negative glow by resonance-radiation transport.

Recent experimental work using optical diagnostics has shown that the peak Hg^+ density in the negative glow is approximately five times higher than the Hg^+ density in the positive column [3]. The peak excited-Hg-atom density in the negative glow was also shown to be approximately half as large as in the positive column [3]. These observations strongly suggest that the multistep ionization mechanism which dominates Hg^+ production in the positive column is not important in the negative glow. Another ionization mechanism produces Hg^+ in the negative glow. The absolute Ar* density (normalized to experiment) from the simulation and the Penning ionization rate [4] for Ar* colliding with ground-state Hg are used to determine production rate per unit volume or source function for Hg^+ in a second simulation. This source function is combined with a Green's-function solution to the ambipolar-diffusion equation for Hg^+ transport in order to study the contribution of Penning ionization to the Hg^+ density in the negative glow. Our predicted Hg^+ absolute density is then compared to measurements of the Hg^+ absolute density. The peak absolute value and the approximate spatial dependence of the simulated Hg^+ density agree with experiment. We conclude that Penning ionization is an important, possibly the dominant, ionization mechanism in the negative glow.

II. EXPERIMENT

Figure 1 is a schematic of the experiment. The Hg-Ar glow-discharge tube is similar to a commercial fluorescent lamp, but it has no phosphor. It is made of fused silica with an inside diameter of 35 mm and is filled with 2.5 Torr of Ar. The hot cathode is a small double-coiled tungsten wire coated with an emission mix which includes Ba, Sr, and Ca oxides to enhance electron emission. This cathode design as well as the lamp diameter and gas fill are typical of commercial lamps. The Hg density is controlled by a water jacket which maintains a cold spot temperature of 40 °C. Warm air blown on the cathode end of the lamp is used to prevent Hg condensation in the cool negative glow region.

The Hg-Ar lamp current is fixed at 400 mA dc in these experiments. This current is chosen because it is near standard operating conditions. Although our data at other currents will not be reported in this paper, it is worth mentioning that the Ar* density is independent of

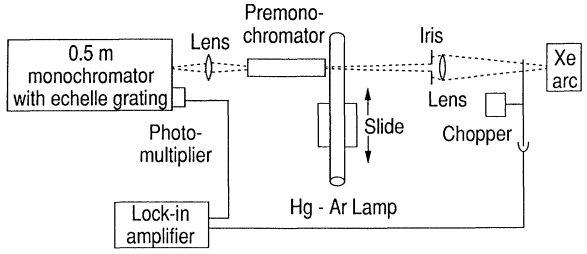

FIG. 1. Schematic of the experiment.

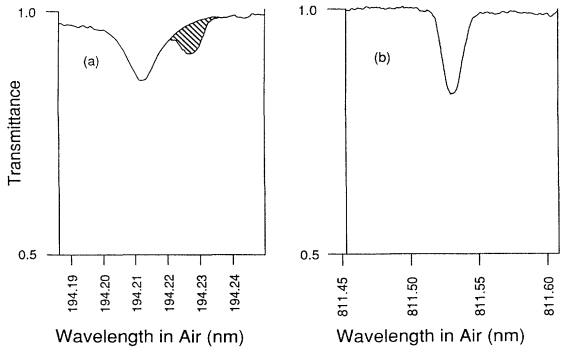

FIG. 2. (a) Sample absorption spectrum at 194 nm for the Hg^+ ion. The cross-hatched region is the equivalent width of the 194.23-nm line of Hg^+. Absorption from the 194.21-nm line of O_2 in the unflushed regions of the optical path is also visible. (b) Sample absorption spectrum at 811.5 nm for the $3p^5 4s\ ^3P_2^\circ$ level of Ar.

current after the density saturates at very low currents (< 10 mA). We suggest that the saturation and current independence of the Ar* density is due to slight variations in the cathode fall voltage. The current dependence of the Hg^+ density in the negative glow has been reported and discussed previously [5].

A very stable (Hamamatsu Super-Quiet) Xe arc lamp is used as a continuum source for these absorption experiments. The radiation from the Xe arc lamp is chopped for phase-sensitive detection before it traverses the Hg-Ar glow-discharge lamp. Phase-sensitive detection makes it possible to discriminate against line emission from the glow discharge and to detect only the continuum emission from the arc discharge with absorption features after it has traversed the glow discharge. After passing through the glow discharge the continuum radiation is filtered by a pre-monochromator and a 0.5-m-focal-length echelle monochromator and then is detected using a photomultiplier (PMT). An echelle monochromator is used because of its superior luminosity-resolution product. The echelle grating is a 316-groove/mm, 63° blaze grating which is used in orders ranging from 7th for the Ar lines near 800 nm to 29th for the Hg^+ line at 194.2 nm. A small low-resolution monochromator (or interference filter) is necessary as a premonochromator due to the small free spectral range of the echelle grating at high orders. Finally the output of the PMT is sent to a lock-in amplifier and the transmittance as a function of frequency is recorded on a chart recorder. This simple experiment is useful from the vacuum ultraviolet to the infrared.

Sample absorption signals at 194.2 nm from ground-state Hg^+ and at 811.5 nm from the $3p^5 4s\ ^3P_2^\circ$ level of Ar are shown in Fig. 2. The 194.23-nm absorption line from Hg^+ is cross hatched, as it lies on the shoulder of an O_2 line at 194.21 nm in the Schumann-Runge band which was analyzed by Curry and Herzberg [6]. In order to reduce the strength of the O_2 absorption line we flush the 0.5-m monochromator and the small premonochromator with dry N_2. The remaining O_2 absorption is from the unflushed regions (total path < 50 cm) around the Xe arc lamp, the mechanical chopper, and the Hg-Ar lamp. It is worth noting that the echelle monochromator can resolve much of the hyperfine and isotopic structure of Hg and Hg^+ lines, although it is not always necessary or desirable to do so in the absorption experiments [3].

The area of the cross-hatched region in Fig. 2(a) divided by the full-scale transmittance is an equivalent width. An equivalent width is directly proportional to the column density of absorbing ions or atoms if the absorption is weak ($< 10\%$) at line center. In such cases the equivalent width, expressed in units of frequency, can be divided by $\pi r_e c f_a$ to determine the number of ions or atoms per unit area along the absorption path, where r_e is the classical radius of the electron, c is the speed of light, and f_a is the absorption oscillator strength.

All of the absorption data in this investigation are analyzed using curves of growth. A curve of growth is the more general relationship between the equivalent width and the column density of ions or atoms. Curves of growth for the 194.2-nm line of Hg^+ and for many lines from the $3p^5 4s$ to the $3p^5 4p$ configuration of Ar are calculated. A value of 0.16 is used for the absorption oscillator strength of the 194.2-nm line of Hg^+. This value is an average of the 0.17 theoretical value from Migdalek and Baylis [7], and the 0.15 experimental value by Bruneteau *et al.* [8]. Oscillator strengths of the Ar lines are from Wiese *et al.* [9]. The hyperfine and isotopic structure of the 194.2-nm line of Hg^+ is included in calculating the curve of growth [10]. A full Voigt profile including the natural or radiative broadening, the pressure broadening, and Doppler broadening at 40 °C is used in calculating all curves of growth. The natural width of the 194.2-nm Hg^+ line is given by the previously mentioned oscillator strength. The natural widths of the various Ar lines are determined from the previously mentioned transition probabilities [9] and from the transition probabilities of the resonance lines. The resonance-transition probabilities, which contribute to the widths of the $3p^5 4s\ ^3P_1^\circ$ and $3p^5 4s\ ^1P_1^\circ$ levels, are from Wiese, Smith, and Glennon [11]. The contribution of pressure broadening to the Lorentzian width in the Voigt profile for the 194.2-nm line of Hg^+ is estimated to be equal to natural broadening. The pressure-broadening coefficient for the 811.5-nm line from the $3p^5 4s\ ^3P_2^\circ$ of Ar is from Lee, Camm, and Copley [12]. The pressure-broadening coefficients of the 801.4-nm line from the $3p^5 4s\ ^3P_2^\circ$ level, the 794.8-nm line from the $3p^5 4s\ ^3P_0^\circ$ level, and the 840.8-

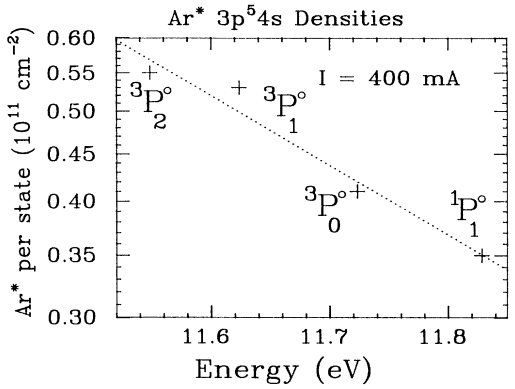

FIG. 3. Column density per state for the $3p^5 4s\ ^3P_2^\circ$, $^3P_1^\circ$, $^3P_0^\circ$, and $^1P_1^\circ$ as a function of energy. The least-squares fit line through the data gives an electron temperature of $k_B T_e = 0.58$ eV.

and 750.4-nm lines from the $3p^5 4s\ ^1P_1^\circ$ level are from Copley and Camm [13]. The pressure-broadening coefficient for the 842.5-nm line from the $3p^5 4s\ ^3P_1^\circ$ level is estimated to be the same as the coefficient for other lines from this lower level [13]. The useful regions of the curves of growth are at most a factor of 2 below a linear extrapolation of the linear (low-density) region. This corresponds to a line-center transmittance greater than exp(−7). Doppler broadening dominates the Voigt profile this close to the linear region of the curve of growth. In order to use only regions near the linear region of each curve of growth it was necessary to use several different lines from some Ar levels. This approach produces the most reliable results over the entire range of Ar* densities.

All densities from absorption measurements are actually column densities because the measurements represent integrals along a line of sight perpendicular to the axis of the cylindrical Hg-Ar lamp. The measurements are reported in units of cm^{-2}. A precision mechanical slide is used to translate the Hg-Ar lamp. Some absorption measurements are made along diameters (on-axis chords). The location of these measurements is specified by the distance z along the tube axis between the hot spot on the cathode and the intersection of the diameter and the tube axis. This coordinate is z in a standard cylindrical coordinate system. Absorption measurements are also made along off-axis chords. The location of these measurements is specified by the z coordinate mentioned previously and by a second coordinate. The second coordinate ρ is the minimum distance between the chord and the tube axis.

Figure 3 shows the relative population per state of the $3p^5 4s\ ^3P_2^\circ$, $^3P_1^\circ$, $^3P_0^\circ$, and $^1P_1^\circ$ levels versus the excitation energy of these levels. It is important to note that all levels have similar populations per state. This figure suggests that the relative populations of levels in the $3p^5 4s$ configuration are approximately in thermal equilibrium with an effective temperature ($k_B T_e = 0.58$ eV) related to average energy of the electrons. The observation that the electron collision rate overwhelms diffusion of the true metastable levels $^3P_2^\circ$ and $^3P_0^\circ$ is not surprising. The resonant levels $^3P_1^\circ$ and $^1P_1^\circ$ have vacuum radiative-decay rates of 1.19×10^8 and 5.1×10^8 sec^{-1}, respectively [11]. Radiation trapping results in a much smaller effective de-

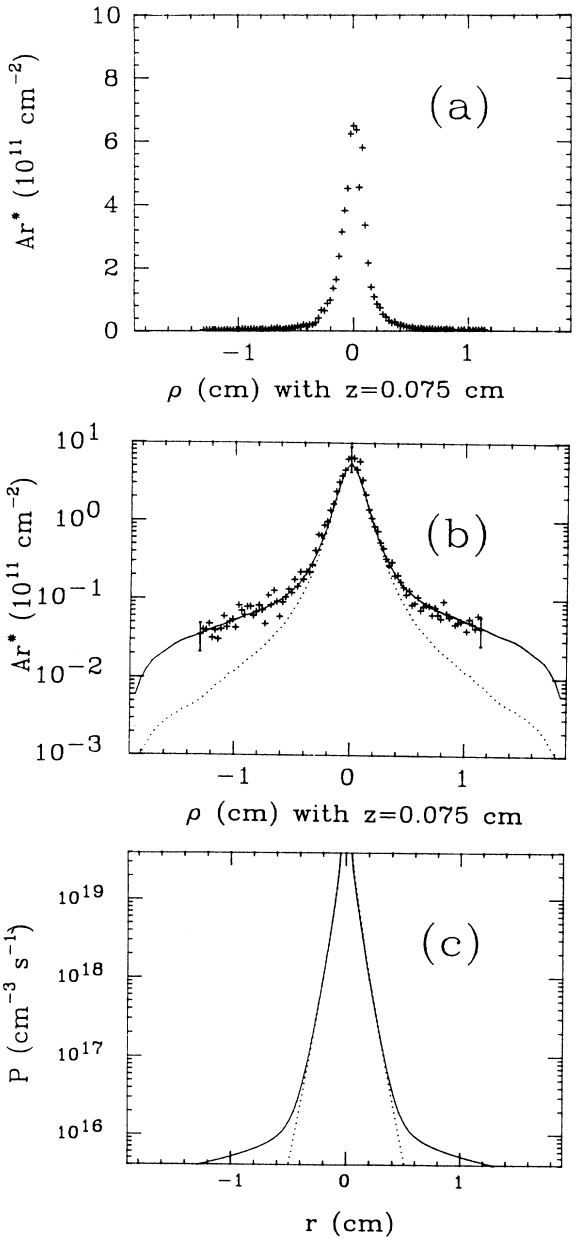

FIG. 4. The crosses are the excited-argon column densities measured perpendicular to the lamp axis and offset from the center of the cathode by $z = 0.075$ cm. (a) Column density on a linear scale. (b) Column density on a logarithmic scale. The error bars represent the dominant, random uncertainty in our measurements. The dotted line is the column density from the simulation using P_1 as the production function. The solid line is the column density from the simulation using P_2 as the production function. (c) Production function used in the simulations. The dotted line is $P_1(r) = (4.0\times10^{18}\ cm^{-2}\,sec^{-1})\exp[(-15\ cm^{-1})r]/r$ and the solid line is $P_2(r) = (3.9\times10^{18}\ cm^{-2}\,sec^{-1})\{\exp[(-15\ cm^{-1})r] + 1.3\times10^{-3}\}/r$.

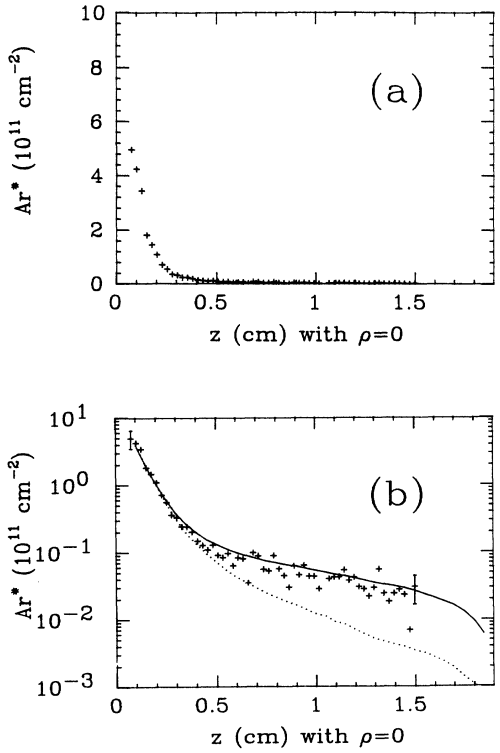

FIG. 5. The crosses are the excited-argon column density measured through diameters of the lamp ($\rho=0$) with the cathode centered at $z=0.0$ cm. (a) Column density on a linear scale. (b) Column density on a logarithmic scale. The error bars represent the dominant, random uncertainty in our measurements. The dotted line is the column density from the simulation using P_1 as the production function. The solid line is the column density from the simulation using P_2 as the production function.

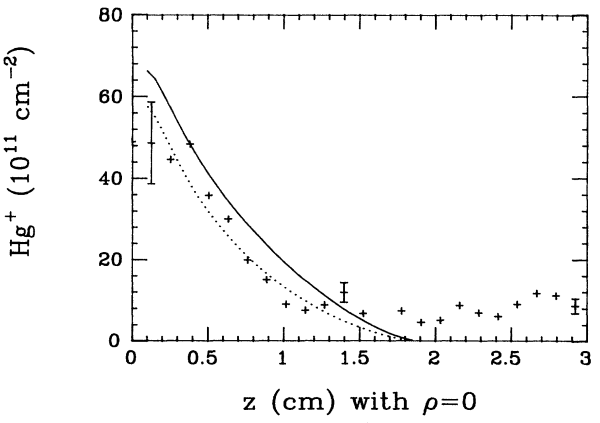

FIG. 6. The crosses are measurements of the mercury-ion column density taken through diameters of the lamp ($\rho=0$). The error bars represent the dominant, random uncertainty in our measurements. The dotted line shows the mercury-ion column density from the simulation using P_1 as the production function. The solid line is the column density from the simulation using P_2 as the production function.

cay rate for these levels. The rate constants for transferring population between levels of the $3p^5 4s$ configuration are as large as $(4-7)\times10^{-7}$ cm^3 sec^{-1} [14]. Electron collisions can overwhelm the trapped radiative-decay rate and equilibrate the relative populations in the $3p^5 4s$ configuration. These observations justify our approximation of representing all of the levels in the $3p^5 4s$ configuration by a single composite excited Ar level. Any Ar atom in the $3p^5 4s$ configuration is represented by Ar*.

Figures 4 and 5 show the Ar* absolute column-density measurements. In these figures (a) is a linear plot and (b) is a semilogarithmic plot. The (z,ρ) coordinates specify the location of each measurement. These plots show the large peak in the Ar* distribution near the cathode hot spot which is on the tube axis. The spatial resolution of these measurements is 0.5 mm in the z direction and is 0.75 mm in the ρ direction. Some of these Ar* density measurements are from a lamp with a glass envelope. Our lamps with fused silica envelopes are used sparingly for experiments in the ultraviolet and vacuum ultraviolet. Figure 6 shows the Hg^+ absolute column-density measurements.

III. SIMULATION OF THE Ar* DENSITY

The balance equation for the Ar* density M is

$$0\equiv\frac{dM}{dt}=P-A_eM-UMN_{\mathrm{Hg}}+A_e\int M(\mathbf{r}')G_M(\mathbf{r},\mathbf{r}')d^3r' \quad (1)$$

In subsequent paragraphs we define each term of this balance equation and describe our solution of the equation for comparison to the experimental Ar* densities.

The primary production rate per unit volume $P(\mathbf{r})$ has a spatial dependence which is sharply peaked near the cathode hot spot. Primary production is due to electron-impact excitation of ground-state Ar by the primary electrons. These electrons are emitted by the cathode and are accelerated by the very thin ($\ll 1$ mm) cathode fall to an average energy near the first excitation energy (11.5 eV) of Ar. The effective vacuum radiative-decay rate of atoms in the $3p^5 4s$ configuration, $A_e=1.23\times10^8$ sec^{-1}, is determined from the vacuum decay rates of the resonant $^3P_1^\circ$ and $^1P_1^\circ$ levels using a statistical (thermal-equilibrium) average over the configuration.

The rate constant $U=9\times10^{-10}$ cm^3 sec^{-1} is for Penning collisions between Ar* and ground-state Hg [4]. Here N_{Hg} is the density of ground-state Hg which we approximate as 1.88×10^{14} cm^{-3}. This assumed value is the equilibrium value at 40 °C. We are neglecting the effects of cataphoresis which might increase N_{Hg} and of temperature gradients which might decrease N_{Hg} near the cathode.

The last term of Eq. (1) represents resonance-radiation transport. This integral term involves a function G_M, which gives the probability that the radiative decay of a resonance atom at $\mathbf{r}'$ produces a photon which is subsequently absorbed at $\mathbf{r}$ to produce a resonance atom. Equation (1) is solved using a Monte Carlo simulation,

thus it is not necessary to give an explicit expression for G_M.

We have considered other mechanisms which could contribute terms to Eq. (1) and found that these mechanisms are negligible. The rate of collisions between pairs of Ar* is small in comparison to the Penning ionization rate. The cross section for the Penning process, represented by the rate constant U, is actually quite large, $\sim 2\times 10^{-14}$ cm^2, which is comparable to the expected cross section for collisions between pairs of Ar* [4]. This means the Penning process will dominate quenching by collisions between pairs of Ar* because M is much less than N_{Hg}. The rate of Ar* quenching from superelastic electron collisions to the ground state is calculated using the rate constant from Gerasimov and Petrov [15]. It is much smaller than the Penning ionization rate $UN_{\mathrm{Hg}}=1.7\times 10^5$ sec^{-1}. The rate of electron-impact ionization of Ar* is estimated using the theoretical cross section by Hyman [16], a Maxwell Boltzmann electron-energy distribution with $k_B T_e=0.58$ eV, and an electron density of 2×10^{12} cm^{-3}. The estimated rate, 50 sec^{-1}, is actually a lower limit because it does not include multistep processes and the non-Maxwellian "tail" electrons in the electron-energy distribution. Nevertheless, the estimated rate is so much smaller than the Penning rate that the process can be neglected. Finally, it is worth mentioning that the diffusion coefficients for Ar metastable atoms and rate constants for quenching of Ar metastable atoms by collisions with ground-state Ar atoms are known [17]. Both of these processes are negligible.

Of the terms in Eq. (1), the source term $P(\mathbf{r})$ is the one we know the least about. It depends on the electron current from the hot spot, and it depends critically on the cathode-fall voltage. For these reasons, we let the spatial distribution and the magnitude of $P(\mathbf{r})$ be adjustable parameters in the Monte Carlo simulation. The spatial distribution and the magnitude of $P(\mathbf{r})$ are adjusted to provide the best possible match to the experimental Ar* densities.

The simulation uses Lorentzian line shapes for the Ar resonance lines at 106.7 and 104.8 nm. The width of the Lorentzian line shapes include the natural widths determined from the vacuum radiative-decay rates of the $^3P_1^\circ$ and $^1P_1^\circ$ levels [11], and include pressure broadening calculated from the formula given by Corney [18]. A ground-state Ar density of 8.05×10^{16} cm^{-3} is used. Simulations are run using both the full Voigt profile and the pure Lorentzian profile. The resulting differences between simulations using these two profiles, if all other parameters are identical, are at most a few percent.

The geometry is also simplified in the Monte Carlo simulations. Although the Hg-Ar lamp has a cylindrical geometry, the cathode breaks the simple cylindrical symmetry. A concentric spherical geometry is used in the simulations because the cathode hot spot is very small in comparison to the tube radius. The cathode is approximated as an inner spherical absorbing boundary with a radius of 0.5 mm. The lamp wall is approximated as an outer spherical absorbing boundary with a radius of 19 mm. One-dimensional geometry, with radial coordinate r measured from the center of the spheres, greatly simplifies the simulation of the radiation transport and the calculation of the Hg^+ transport described in Sec. IV. Unfortunately, this approximation limits the comparison of simulation results and experiment to regions near the hot spot. The one-dimensional simulations are adequate for addressing issues such as the ionization balance of the negative glow, but are inadequate for studying the transition from the negative glow to the Faraday dark space.

In order to compare simulated Ar* densities and experimental Ar* column densities, we perform a line-of-sight integration through the spherically symmetric distribution from the simulation. The minimum distance between the line of sight and the center of sphere is taken to be equivalent to $(z^2+\rho^2)^{1/2}$ in the experiment.

The results of the simulations for a number of different assumptions about the production rate per unit volume P convince us that the high-density part of the experimental Ar* density maps is approximately a map of the actual production rate per unit volume in the lamp. This conclusion agrees with earlier studies by Phelps on a related problem [19]. The linear plots of the Ar* density in Figs. 4(a) and 5(a) provide the approximate spatial dependence of P.

A good fit to the Ar* density measurements in the central high-density region is achieved using a production rate per unit volume of

$$P_1(r)=(4.0\times 10^{18}\ \mathrm{cm}^{-2}\mathrm{sec}^{-1})\exp[(-15\ \mathrm{cm}^{-1})r]/r \tag{2}$$

in the radiation-transport simulations. This choice for $P(r)$ corresponds to a total spatially integrated production rate of 1.5×10^{16} sec^{-1}. The simulation results corresponding to this choice for $P(r)$ are given as the dotted lines in Fig. 4(b) and 5(b). This simulation is in agreement with the measured Ar* column density in the central region, but the simulated Ar* density is too low in the "wings" (at large r). An excellent overall fit to the Ar* density measurements is achieved using

$$P_2(r)=(3.9\times 10^{18}\ \mathrm{cm}^{-2}\mathrm{sec}^{-1})\times\{\exp[(-15\,\mathrm{cm}^{-1})r]+1.3\times 10^{-3}\}/r\ . \tag{3}$$

This choice for $P(r)$ corresponds to a total spatially integrated production rate of 2.3×10^{16} sec^{-1}. This total production rate corresponds to 1% of the primary electrons ($\sim$400 mA) producing an excited Ar atom. The optimum simulation results corresponding to this choice for $P(r)$ are given as the solid line in Figs. 4(b) and 5(b). Figure 4(c) is a plot of the two choices for $P(r)$.

The Ar* spatial distribution for a particular choice of P is also sensitive to the Penning ionization rate. For example, if P_1 is used with a reduced Penning ionization rate, then the wings increase and approach the experimental densities. The Penning rate constant of 9×10^{-10} cm^3 sec^{-1} from Wren and Setser [4] is much larger than the rate constant of 1.3×10^{-10} cm^3 sec^{-1} measured by Phelps and Molnar [17]. We cannot provide a definitive explanation for the large difference between the measurements, although Wren and Setser suggest that Phelps and Molnar may not have accurately determined the Hg density in their experiment [4,17]. Both papers report Pen-

ning ionization rate constants for the true metastable levels $3p^5 4s\ ^3P_2^\circ$ and/or $^3P_0^\circ$. The resonance Ar atoms in the $3p^5 4s$ configuration are undoubtedly more reactive than the true metastable atoms because of their longer-range interaction. A weighted-average Penning ionization rate constant which includes both metastable and resonance atoms is needed for modeling our experiment, thus we use the larger rate constant from Wren and Setser's measurement. In the optimum simulations 69% of the Ar* atoms produced in the negative glow ultimately (after many emission-absorption cycles) decay via Penning ionization. An additional 3.9% ultimately produce resonance photons which are absorbed by 0.5-mm-radius cathode. The balance ultimately produce photons which are absorbed by the 19-mm-radius wall.

IV. SIMULATION OF THE Hg^+ DENSITY

The balance equation for the Hg^+ density (assumed to be the same as the electron density) is

$$0 \equiv \frac{dn_e}{dt} = UMN_{\mathrm{Hg}} + D_{\mathrm{amb}} \nabla^2 n_e \ . \tag{4}$$

The source term is the production rate per unit volume for Penning ionization UMN_{Hg} from the optimum simulation described in the preceding section. The loss term is the ambipolar diffusion term $D_{\mathrm{amb}} \nabla^2 n_e$. An electron temperature $k_B T_e = 0.58$ eV is combined with Hg^+ mobilities in Ar measured by Chanin and Biondi to determine the diffusion coefficient D_{amb} [20]. We neglect gradients in the electron and gas temperature.

The balance equation we use for the Hg^+ density does not include single-step electron-impact ionization of Hg by the primary electrons. These electrons are emitted by the cathode with some distribution which reflects the cathode temperature, the patch effect, and possibly other phenomena. The primary electrons are accelerated by the very thin ($\ll 1$ mm) cathode fall to an average energy near the first excitation energy (11.5 eV) of Ar. The ionization energy of Hg is 10.4 eV. The relative importance of single-step ionization of Hg vs Penning ionization from Ar excitation is dependent on the shape of the electron-energy distribution function above 10.4 eV.

Our preliminary simulations of the primary electron-energy distribution function indicate that the rate of single-step electron-impact ionization of Hg is comparable to the rate of electron-impact excitation of Ar. These preliminary kinetic-theory simulations will not be reported here. More sophisticated simulations are planned. In this work we neglect single-step ionization of Hg and explore what fraction of the observed Hg^+ density can be accounted for using only Penning ionization.

The spherical geometry with radial coordinate r, as used in the radiation transport simulation, is compatible with a Green's-function solution to Eq. (4). For this problem the Green's function is

$$G_n(r,r') = (1 - 0.5\ \mathrm{mm}/r_<) \times (1/r_> - 1/19\ \mathrm{mm})/[4\pi D_{\mathrm{amb}}(1 - 0.5/19)] \ . \tag{5}$$

Here $r_<$ is the lesser of r and r', while $r_>$ is the greater of r and r'. A straightforward numerical integral of the product of G_n and the source term over all r' yields the density n_e as function of r. The simulated Hg^+ density is compared to experimental results in Fig. 6. Extraordinarily good agreement between the measured Hg^+ densities and the simulation results is obtained. In the optimum simulation, which is represented by the solid line, 18% of the Hg^+ ions diffused to cathode and the balance diffused to the outer spherical wall. This simulation also implies a field reversal ~ 1 mm from the cathode.

V. SUMMARY AND CONCLUSION

In summary, the absolute densities of excited Ar atoms and ground-state Hg^+ ions are mapped using absorption spectroscopy in the negative glow of a hot-cathode Hg-Ar discharge. The Ar* density is sharply peaked near the cathode hot spot and has a low but nonzero value throughout the negative glow. This distribution is consistent with resonance radiation transport of the Ar excitation from a localized production region near the cathode hot spot to the rest of the negative glow. A Monte Carlo simulation of the radiation trapping is found to agree with the measured Ar* column densities.

The Hg^+ density is quite high in the negative glow. Earlier measurements show that the Hg^+ density is five times higher in the negative glow than it is in the positive column at 400 mA current. The density of excited Hg atoms is lower in the negative glow than in the positive column. These two observations strongly suggest that the multistep ionization of Hg, which dominates ion production in the positive column, is not important in the negative glow. A simulation of the Hg^+ kinetics and transport in the negative glow is found to be in excellent agreement with the measured Hg^+ column density. The Hg^+-ion simulation uses the product of the Ar* density and a rate for Penning ionization as a source term or production rate per unit volume. Ambipolar diffusion is used to describe ion transport in the negative glow. Although a large rate constant for Penning ionization is used in the simulation, we think it is reasonable because the Ar* density is a mixture of true metastable Ar atoms and the more reactive resonance Ar atoms.

The major conclusion from this study is that Penning ionization is an important, possibly the dominant, ionization mechanism in the negative glow. This ionization mechanism is consistent with both the absolute Hg^+ density and spatial distribution. The ion-production rate per unit volume has a spatial dependence which follows the Ar* density and is large very close to the cathode hot spot. The resulting Hg^+ density also peaks near the cathode hot spot. These observations imply an electric-field reversal in the negative glow within ~ 1 mm of the cathode hot spot.

The goal of continuing work on this problem is to develop a quantitative understanding of the power balance of the hot cathode. The important terms in the power balance of the hot cathode are given in a classic model by Waymouth [2]. A more detailed quantitative understanding should emerge from a combination of experimental

work using advanced diagnostics and from more sophisticated simulations.

ACKNOWLEDGMENTS

The research is supported by the General Electric Company. We are grateful to Dr. John Anderson of General Electric. His corporate research reports influenced the course of our investigation. Dr. Doug Doughty from General Electric and Mr. Jianou Shi of Penn State helped with data collection during visits to Wisconsin.

[1] See, for example, J. T. Dakin and L. Bigio, J. Appl. Phys. **63**, 5270 (1988).
[2] J. F. Waymouth, *Electric Discharge Lamps* (MIT Press, Cambridge, MA, 1971).
[3] R. C. Wamsley, J. E. Lawler, J. H. Ingold, L. Bigio, and V. D. Roberts, Appl. Phys. Lett. **57**, 2416 (1990).
[4] D. J. Wren and D. W. Setser, J. Chem. Phys. **74**, 2331 (1981).
[5] R. C. Wamsley, T. R. O'Brian, K. Mitsuhashi, and J. E. Lawler, Appl. Phys. Lett. **59**, 2947 (1991).
[6] V. J. Curry and G. Herzberg, Ann. Phys. (Leipzig) **19**, 800 (1924).
[7] J. Migdalek and W. E. Baylis, J. Quant. Spectrosc. Radiat. Transfer **22**, 113 (1979).
[8] A. M. Bruneteau, A. M. Icole, C. Rouille, A. Poquerusse, and H. J. Doucet, Phys. Lett. A **46**, 309 (1974).
[9] W. L. Wiese, J. W. Brault, K. Danzmann, V. Helig, and M. Kock, Phys. Rev. A **39**, 2461 (1989).
[10] Y. Guern, A. Bideau-Mehu, R. Abjean, and A. Johannin-Gilles, Phys. Scr. **14**, 273 (1977).
[11] W. L. Wiese, M. W. Smith, and B. M. Glennon, *Atomic Transition Probabilities: Vol. II Sodium Through Calcium,* Natl. Stand. Ref Data Ser. **22**, U.S. Natl. Bur. Stand. (U.S. GPO, Washington, DC, 1966), p. 192.
[12] C. S. Lee, D. M. Camm, and G. H. Copley, J. Quant. Spectrosc. Radiat. Transfer **15**, 211 (1975).
[13] G. H. Copley and D. M. Camm, J. Quant. Spectrosc. Radiat. Transfer **14**, 899 (1974).
[14] O. P. Bochkova, E. A. Sukiasyan, and Yu. A. Tolmachev, Opt. Spektrosk. **38**, 185 (1975) [Opt. Spectrosc. (USSR) **38**, 104 (1975)].
[15] G. N. Gerasimov and S. Ya. Petrov, Opt. Spectrosk. **43**, 18 (1977) [Opt. Spectrosc. (USSR) **43**, 7 (1975)].
[16] H. A. Hyman, Phys. Rev. A **20**, 855 (1979).
[17] A. V. Phelps and J. P. Molnar, Phys. Rev. **89**, 1202 (1953).
[18] A. Corney, *Atomic and Laser Spectroscopy* (Clarendon, Oxford, 1977), p. 262.
[19] A. V. Phelps, Phys. Rev. **110**, 1362 (1958).
[20] L. M. Chanin and M. A. Biondi, Phys. Rev. **107**, 1219 (1957).